Open-top Bessel beam two-photon light sheet microscopy for three-dimensional pathology

Running title: OT-TP-LSM for 3D pathology

Won Yeong Park[1], Jieun Yun[1], Jinho Shin[3], Byung Ho Oh[4], Gilsuk Yoon[5], Seung-Mo Hong[6], and Ki Hean Kim[1, 2, *]

[1] Department of Mechanical Engineering, Pohang University of Science and Technology, Pohang, Gyeongsangbuk, 37673, Republic of Korea.

[2] Department of I-Bio, Pohang University of Science and Technology, Pohang, Gyeongsangbuk, 37673, Republic of Korea.

[3] Department of Medicine, University of Ulsan College of Medicine, Seoul, 05505, Republic of Korea.

[4] Department of Dermatology, College of Medicine, Yonsei University, Seoul, 03722, Republic of Korea.

[5] Department of Pathology, School of Medicine, Kyungpook National University, Daegu, 41944, Republic of Korea.

[6] Department of Pathology, Asan Medical Center, University of Ulsan College of Medicine, Seoul, 05505, Republic of Korea.

*Corresponding authors

Ki Hean Kim

Department of Mechanical Engineering and

Division of Integrative Biosciences and Biotechnology

Pohang University of Science and Technology (POSTECH)

Mechanical Laboratory Building 212, 77 Cheongam-ro, Nam-gu,

Pohang, Gyeongbuk 37673, Republic of Korea

Phone No: 82-54-279-2190

Email Address: kiheankim@postech.ac.kr

Keywords: nondestructive pathology, 3D pathology, two-photon light sheet microscopy, Bessel beam illumination, 3D imaging, unsupervised deep learning

Abstract

Nondestructive pathology based on three-dimensional (3D) optical microscopy holds promise as a complement to traditional destructive hematoxylin and eosin (H&E) stained slide-based pathology by providing cellular information in high throughput manner. However, conventional techniques provided superficial information only due to shallow imaging depth. Herein, we developed open-top two-photon light sheet microscopy (OT-TP-LSM) for intraoperative 3D pathology. An extended depth of field two-photon excitation light sheet was generated by scanning a nondiffractive Bessel beam, and selective planar imaging was conducted with cameras at 400 frames/s max during the lateral translation of tissue specimens. Intrinsic second harmonic generation was collected for additional extracellular matrix (ECM) visualization. OT-TP-LSM was tested in various human cancer specimens including skin, pancreas, and prostate. High imaging depths were achieved owing to long excitation wavelengths and long wavelength fluorophores. 3D visualization of both cells and ECM enhanced the ability of cancer detection. Furthermore, an unsupervised deep learning network was employed for the style transfer of OT-TP-LSM images to virtual H&E images. The virtual H&E images exhibited comparable histological characteristics to real ones. OT-TP-LSM may have the potential for histopathological examination in surgical and biopsy applications by rapidly providing 3D information.

Introduction

Conventional histopathological examination using thin sectioning and hematoxylin and eosin (H&E) staining has inherent limitations, including long processing time, tissue loss, sampling error, limited two-dimensional (2D) information, and artifacts. High-speed three-dimensional (3D) optical microscopy, which can visualize cellular structures without thin sectioning, holds promise for nondestructive 3D pathological examination [1-4]. Various high-speed 3D microscopy techniques have been developed [5-12], and open-top light sheet microscopy (OT-LSM) is a promising technique that enables high-throughput imaging with sheet illumination and planar imaging on uneven tissue surfaces [13-16]. OT-LSM is a specialized form of LSM for imaging large tissue specimens such as biopsy specimens by placing all the optical components below the sample holder. However, fluorescence 3D microscopy techniques, including OT-LSM, have shallow imaging depths in turbid tissue owing to high excitation light scattering and absorption, which limits precise 3D histopathology. As alternative method for high depth imaging, two-photon microscopy (TPM) has been used [17-19]. TPM is based on nonlinear excitation of fluorophores and achieves high imaging depths up to a few hundred micrometers by using long excitation wavelengths, which reduce light scattering. Furthermore, TPM provides additional intrinsic second harmonic generation (SHG) contrast for imaging collagen in the extracellular matrix (ECM) [20-22]. Two-photon LSM (TP-LSM) techniques have been developed for high-speed and high-depth imaging of live small animals and biological studies [23-27], but they were not in an open-top configuration.

In this study, we present the development of an open-top TP-LSM (OT-TP-LSM) with a Bessel beam for high-throughput and high-depth 3D pathological examination of large biopsied tissue specimens. A nondiffractive Bessel beam was used for the generation of an extended depth of field (EDOF) excitation light sheet with minimal side lobe effects [28, 29].

High imaging depths were achieved by using long excitation wavelengths and fluorescent nuclear probes emitting relatively long wavelengths. After development and characterization, the system was applied to high-throughput 3D imaging of various human cancer specimens, including skin, pancreas, and prostate in comparison with conventional H&E stained images for verification. Moreover, OT-TP-LSM images were converted to virtual H&E images using deep learning style transfer. We demonstrate that OT-TP-LSM imaging is comparable to that obtained from H&E stained slides for several human cancer types and has the potential for rapid and accurate nondestructive 3D pathology.

Results

Open-top two-photon light sheet microscopy (OT-TP-LSM) for 3D pathology

Schematics and characterization results of OT-TP-LSM are presented in Figure 1. OT-TP-LSM is an orthogonally arranged dual objective LSM with a liquid prism interface (Figure 1A). All optical components of OT-TP-LSM were positioned underneath a sample holder to accommodate large size specimens without physical interference with the illumination and imaging optics. Two 20x air objective lenses with a moderate numerical aperture (NA) of 0.42 were used to deliver a thin excitation light sheet and collect emission light efficiently. The custom liquid prism was used to transmit excitation light into the specimen and to collect emission light out with minimal aberration by refractive index (RI) matching with different mediums where the sample was immersed (Figure 1B). The liquid prism was filled with diluted glycerol in distilled water, whose RI was matched to that of a quartz (RI: 1.45) window in a sample holder. A Ti-Sapphire laser beam was expanded and converted to a Bessel beam using an axicon lens. The Bessel beam was reflected on a galvanometer scanner and relayed to the sample through the liquid prism by a combination of a tube lens and an objective lens. The scanner scanned the Bessel beam to form an EDOF excitation light sheet.

103 Emission light generated by the sample was collected by the imaging objective lens through
104 the liquid prism, split into two channels, one for fluorescence and the other for SHG, using a
105 dichroic mirror, and imaged simultaneously by two scientific complementary metal-oxide–
106 semiconductor (sCMOS) cameras with individual gain control.

107 The excitation light sheet was designed to have a DOF of 180 μm with a thickness of
108 0.9 μm (Figure 1 - figure supplement 1). The imaging field of view was 600 μm × 170 μm
109 with 2,048 × 512 pixels and was limited by the DOF of the Bessel beam. Emission light
110 scattering in the specimen further limited the imaging depth. Selective planar images along
111 the oblique excitation light sheet were acquired sequentially with a stepwise X-axis
112 translation of the specimen by the motorized stage (Figure 1C). A graphical user interface
113 based on LabVIEW was used to generate trigger signals for both the cameras and the
114 motorized stage. OT-TP-LSM was characterized by imaging fluorescent microspheres (0.5
115 μm in diameter) embedded in agarose gel, whose RI was matched to that of the solution in
116 the liquid prism (Figure 1D). The image throughput was 0.24 mm^2/s at an acquisition rate of
117 400 fps and step size of 1 μm. The image resolution was measured to be 0.9 μm in all
118 dimensions. The lateral resolution in the Y-Z' plane was approximately 128% of the
119 theoretical value due to spherical aberration induced by the RI mismatch between air and the
120 immersion medium, but this was sufficient for detecting cellular features.

121 The imaging depth of OT-TP-LSM was evaluated using freshly excised human skin
122 specimens. Proflavine was topically instilled onto the specimen for nuclear labeling before
123 imaging. A representative Y-Z' plane image is shown in Figure 1E. The imaging depth in the
124 skin was approximately 90 μm in the 45°-tilted image plane, and the actual depth was 64 μm
125 from the surface. To compare the imaging depth, the same skin specimen was imaged using
126 conventional one-photon excitation-based LSM (1PLSM). The imaging depth was
127 approximately 28 μm in the 45°-tilted image plane and 20 μm from the surface, which was

128 approximately three times less than that of OT-TP-LSM. While the imaging depth of OT-TP-
129 LSM was sufficient for visualizing 3D cell structures in the skin, it was relatively low
130 compared to that of conventional point-scanning based TPM due to the effect of emission
131 photon scattering.

132 **3D OT-TP-LSM imaging of human skin cancers**

133 After development and characterization, the performance of OT-TP-LSM was assessed in
134 human skin cancer specimens. Representative OT-TP-LSM images of two basal cell
135 carcinoma (BCC) specimens are presented along with H&E stained histology images in
136 Figure 2. The H&E images were obtained from the same specimens at slightly different
137 depths. The OT-TP-LSM images visualized both cell structures and ECM in the cross-
138 sectioned skin specimens, where proflavine-labeled cell nuclei and SHG-emitting collagen
139 were depicted in green and blue, respectively. A mosaic image of the first BCC specimen
140 visualized the epidermis as a thin layer on the top and the underlying dermis, most of which
141 was occupied by BCC nests (Figure 2A). The epidermis and dermis were easily identifiable
142 with SHG contrasts. Two regions of interest (ROI) were selected in the epidermis and BCC,
143 and magnified images of these ROIs are presented to show the detailed cell structures.
144 Magnified image in the epidermis (ROI 1) showed layered squamous epithelial cells (Figure
145 2B). Squamous cells in the basal layer were relatively large and individually resolved, while
146 those in the upper layers were unresolved with relatively small cytoplasm and appeared as a
147 band. Magnified images of BCC (ROI 2) showed many irregularly shaped tumor nests
148 composed of densely packed monomorphic tumor cells of the same size (Figure 2C).

149 The mosaic image of the second BCC specimen mainly showed two different cell
150 structures in the dermis (Figure 2D). The structures on the right side were BCCs, while those
151 on the left side had intact ECM composition and differed from BCCs. The corresponding
152 H&E stained histology image confirmed these as BCCs and normal gland structures in the

153 dermis, respectively. Two ROIs were selected in the nontumorous skin region, and magnified
154 images at two different depths are presented along with their corresponding H&E stained
155 images. Magnified images of ROI 3 visualized clusters of small round tubular structures
156 (Figure 2E). The image at depth 2 showed a duct structure composed of single-layered
157 cuboidal epithelial cells, which is typical of eccrine glands. Magnified images of ROI 4 at
158 two different depths showed pear-shaped clusters consisting of cells with clear and bulging
159 cytoplasm, which is typical of sebaceous glands (Figure 2F). Using 3D visualization, normal
160 glandular structures in the dermis were distinguished from BCC tumor nests (Video 1). Both
161 eccrine and sebaceous glands could appear similar to BCC nests in 2D images at certain
162 depths. Hence, 3D visualization would be important for distinguishing them.

163 **3D OT-TP-LSM imaging of human pancreatic cancers**

164 We then used OT-TP-LSM to visualize human pancreas specimens including those with
165 pancreatic cancer. Instead of proflavine, propidium iodide (PI) was used as a nuclear labeling
166 agent to increase the imaging depth (Figure 3 - figure supplement 1). The proflavine-labeled
167 pancreas specimens had a relatively shallow imaging depth (up to 30 μm approximately)
168 owing to the dense desmoplastic stromal cell composition. PI labeling allowed for deeper
169 imaging up to approximately 55 μm from the surface due to the longer peak emission
170 wavelength of 640 nm compared to proflavine. PI cytoplasmic labeling also occurred in
171 addition to nuclear labeling of both acinar and neoplastic cells, probably owing to PI labeling
172 of both DNA and RNA (Figure 3 - figure supplement 2) [30, 31]. Cell nuclei were identified
173 with relatively strong fluorescence in the membrane and weaker fluorescence in the core.
174 Representative OT-TP-LSM images and corresponding H&E stained slide images of normal
175 pancreas and premalignant lesion specimens, and a pancreatic cancer (also known as
176 pancreatic ductal adenocarcinoma, PDAC) specimen are shown in Figures 3 and 4,
177 respectively. The mosaic image of the normal pancreas visualized a dense distribution of

178 acini composed of exocrine acinar cells in good correlation with the corresponding H&E
179 image (Figure 3A). Two ROIs were selected, and magnified images are presented to show
180 detailed cytologic features of the normal pancreas. Magnified images of ROI 1 visualized the
181 cellular structure of acini and islets of Langerhans expressing different fluorescence
182 intensities (Figure 3B). Acini were composed of lobules of acinar cells, and the boundaries of
183 the acini were identified with relatively low PI fluorescence. The islets of Langerhans
184 expressed relatively low PI fluorescence, probably due to the high composition of crystallized
185 insulin in beta cells [32]. Magnified images of ROI 2 visualized a duct in the normal pancreas
186 (Figure 3C). The duct was composed of single-layered cuboidal epithelial cells with round
187 nuclei and was surrounded by dense fibrous tissue expressing SHG. The mosaic image of the
188 pancreatic premalignant lesion exhibited different and irregular structures, including dilated
189 ducts with intraductal proliferation of papillary structures (Figure 3D). Two different types of
190 precursor lesions, intraductal papillary mucinous neoplasm (IPMN) and pancreatic
191 intraepithelial neoplasia (PanIN), were observed [33, 34], and tumor cells were tall columnar
192 containing intracytoplasmic mucin [35]. A corresponding H&E histology image confirmed
193 the precursor lesions. Magnified images of PanIN (ROI 3) at two different depths showed
194 proliferation of papillary epithelial cells with intracytoplasmic mucin, and 3D morphology of
195 the PanIN (Figure 3E). OT-TP-LSM images were very similar to the corresponding H&E
196 images, indicating OT-TP-LSM provided comparable histopathological information to that of
197 H&E stained slides without thin sectioning.

198 A mosaic image of the PDAC arising from the IPMN specimen showed various
199 abnormal ductal structures including cancer glands, IPMN, and surrounding pancreatitis,
200 which were confirmed by the corresponding H&E stained slide image (Figure 4A). More
201 desmoplastic fibrous stroma and a few abnormal cancer glands were observed compared to
202 normal pancreas tissue [36, 37]. Two ROIs were selected in the PDAC region and the

203 boundary region with nonneoplastic pancreatitis, and magnified images are presented to show
204 detailed cellular structures. Magnified images of ROI 1 (PDAC) at two different depths
205 showed irregularly shaped glands with sharp angles (Figure 4B). The glands exhibited
206 disorganized cancer cell arrangement with nuclear membrane distortion. Magnified images of
207 ROI 2 showed both nonneoplastic ducts and cancer glands in different cell arrangements
208 (Figure 4C). The nonneoplastic ducts had small, evenly distributed cells with relatively high
209 nuclear fluorescence. Cancer glands, on the other hand, had disorganized and multilayered
210 nuclei.

211 **3D OT-TP-LSM imaging of human prostatic cancers**

212 OT-TP-LSM was used to visualize human prostatectomy specimens, and two representative
213 OT-TP-LSM images of benign and adenocarcinoma specimens are presented in Figure 5. The
214 mosaic image of the histologically confirmed benign prostate showed benign glands
215 dispersed throughout the specimen with relatively weak SHG composition between the
216 glands (Figure 5A). An ROI was selected on benign glands, and magnified images are
217 presented to show cytologic features alongside the corresponding H&E stained slide image
218 (Figure 5B). Multiple cell layers, consisting of secretory cells and basal cells, lined the
219 central lumen in the ducts of benign glands. Although images at two different depths are
220 presented, the cell distribution was similar because of the relatively small depth difference
221 compared to the gland size. The mosaic image of the prostate adenocarcinoma in Figure 5C
222 showed both the benign and cancer regions, whose boundary was marked with a white solid
223 line, and they were confirmed by the corresponding H&E stained image. The cancer region
224 was full of crowded small gland structures, whereas the benign region consisted of relatively
225 large glands surrounded by fibrous stroma. Magnified images of ROI 2 in the cancer region
226 showed small glands composed of monolayered cell walls (Figure 5D). The cancer glands
227 had single-layered malignant secretory cells only due to the loss of basal cell layers. The

228 corresponding H&E histology was diagnosed as Gleason score 3+3 prostatic adenocarcinoma.
229 OT-TP-LSM provided histological information equivalent to that of the H&E stained image
230 without the need for sectioning.

231 **Deep learning-based style transfer for virtual H&E**

232 OT-TP-LSM images visualized histological features with high similarity to those in H&E
233 images, but they may be unfamiliar to pathologists and clinicians accustomed to traditional
234 H&E stained slide histology. PI-labeled OT-TP-LSM images were converted to virtual H&E
235 images using Cycle-consistent generative adversarial network (CycleGAN) [38].
236 Representative virtual H&E images of pancreatic premalignant (PanIN) and PDAC are
237 presented along with the corresponding real H&E stained images for comparison in Figure 6.
238 Mosaic virtual H&E images of both PanIN and PDAC showed similar patterns to the
239 corresponding real H&E stained histology images (Figure 6A, C). Although the normal
240 region in the lower left corner of the virtual PanIN image was not transformed properly
241 possibly due to insufficient image data of normal acini for training (Figure 6A), the
242 magnified virtual H&E images clearly displayed distinct cell distributions of PanIN and
243 PDAC by labeling cell cytoplasm and nuclei in pink and purple, respectively (Figure 6B, D).
244 PanINs were visualized as slightly dilated, irregularly clustered ducts with preserved
245 structural integrity (Figure 6B), whereas PDAC had disorganized cell arrangement with
246 haphazard patterns, infiltrating into the surrounding tissue with desmoplastic stroma (Figure
247 6D). Histological features found in the virtual H&E images were diagnostic factors for the
248 discrimination of PDAC and PanIN. Virtual H&E staining of OT-TP-LSM via CycleGAN
249 could provide comparable cellular information to conventional H&E stained histology.

250

251 **Discussion**

252 OT-TP-LSM was developed to enable rapid and precise 3D pathological examination of
253 excised tissue specimens during both biopsy and surgery, allowing visualization of 3D cell
254 structures. OT-TP-LSM generated a two-photon excitation light sheet using one-dimensional
255 Bessel beam scanning, and planar images were acquired by collecting emission light from the
256 excitation light sheet with sCMOS cameras at 400 fps maximum. Proflavine and PI were
257 used for nuclear labeling and cell structure visualization, and intrinsic SHG contrast was used
258 for ECM visualization. The performance of OT-TP-LSM was characterized in comparison
259 with histopathologic images of H&E stained slides in various human cancer specimens
260 including skin, pancreas, and prostate. 3D OT-TP-LSM images were well matched with the
261 corresponding 2D H&E histological images with all the human tissue specimens used. The
262 relatively high imaging depths of OT-TP-LSM enable the visualization of detailed 3D cell
263 structures with high contrast and without distortion. The high-quality images of OT-TP-LSM
264 may be partially attributed to the use of the nondiffractive Bessel beam for the generation of
265 an EDOF excitation light sheet [39].

266 OT-TP-LSM could visualize 3D cell structures in the skin up to a depth of 60 μm by
267 using long wavelength excitation light and proflavine labeling. Although the imaging depth
268 was not high compared with conventional TPM, it was sufficient to visualize 3D cell
269 structures in the skin without sectioning artifacts. The imaging depth varied depending on the
270 tissue type, and the imaging depths of both pancreas and prostate were relatively shallow in
271 comparison to that of the skin. This low imaging depth could be attributed to the dense cell
272 composition and higher RI than the current immersion medium. To increase the imaging
273 depth, PI with a relatively long emission wavelength was used. Additionally, an immersion
274 medium with 1.5 RI could improve the imaging depth [40], and a quick optical clearing
275 method could also be used to enhance the imaging depth [41].

We applied the unsupervised deep learning network of CycleGAN to PI-labeled OT-TP-LSM images of pancreas specimens to generate virtual H&E images, and the cytoplasm and cell nuclei, which exhibited intensity differences in greyscale, were transformed to H&E-like pseudo colors. Virtual H&E images in pancreatic cancer provided histological features equivalent to the conventional H&E. Although the CycleGAN network showed the potential for virtual H&E staining, further development is necessary to ensure robust performance and universal application. Therefore, CycleGAN will be trained using more OT-TP-LSM image data from different tissue types such as skin and prostate.

The current OT-TP-LSM has several limitations that require improvement. One issue is spherical aberration induced by the RI mismatch between the liquid prism and air when using air objective lenses in both illumination and imaging arms. Spherical aberration degraded the image resolution, particularly in the imaging arm. An immersion imaging objective lens with a high NA would be desirable to improve both image resolution and emission light collection efficiency. The excitation light sheet was generated through the rapid scanning of a single Bessel beam, resulting in a short pixel dwell time compared to that of a conventional single photon 2D light sheet. The generation of excitation light sheet with the scanning of multiple Bessel beams would increase the pixel dwell time and image contrast [42, 43]. The relatively short excitation wavelength of 770 nm was used for all the imaging to efficiently collect additional SHG light [20], but the imaging depth was limited. Longer excitation wavelengths with long emission wavelength probes would increase the imaging depth beyond those presented here.

In conclusion, OT-TP-LSM was developed for high-throughput and high-depth tissue examination. OT-TP-LSM was tested with various human cancers including skin, pancreas, and prostate by visualizing 3D cell structures. Intrinsic SHG contrast was used for visualizing ECM and detecting fibrosis. Normal glands and BCC nests were clearly distinguished, and

both pancreatic and prostate cancers were clearly identified using 3D visualization of cell structures with OT-TP-LSM. Furthermore, virtual H&E staining of OT-TP-LSM using CycleGAN provided histopathologic information comparable to that from H&E stained slides. Therefore, OT-TP-LSM could be useful for rapid and precise nondestructive 3D pathology.

Materials and methods

OT-TP-LSM setup

The schematics of OT-TP-LSM are shown in Figure 1A. As the light source, OT-TP-LSM used a titanium–sapphire pulse laser (Chameleon II, Coherent) with 140-fs pulse width and 80-MHz pulse repetition rate. The excitation wavelength was set at 770 nm for imaging human tissue specimens. In the illumination arm, the laser beam was expanded from 1.4 mm to 1.86 mm and then converted to a Bessel beam by using an axicon lens (131-1270 + ARB825, Eksma). The Bessel beam was relayed onto the specimen through two lens pairs of L1 (AC254-045-B, Thorlabs) and L2 (AC254-080-B, Thorlabs), and L3 (AC254-150-B, Thorlabs) and a 20× air illumination objective lens with 0.42 NA (MY20X-804, Mitutoyo). The Bessel beam diameter at the back aperture of the objective lens was approximately 6.8 mm to prevent beam clipping, and the effective illumination NA was 0.34. The excitation light sheet was generated by Y-axis scanning of the Bessel beam with a galvanometric scanner (GVS102, Thorlabs), which was positioned between L1 and L2. The liquid prism transmitted the excitation light normally through a coverslip (HSU-0101122, Marienfeld Superior), RI-matching solution, and a 0.25 mm thick round quartz window (26043, Ted Pella) at the bottom of the sample holder, and then to the sample (Fig. 1B). Diluted 85% glycerol (Samchun) in distilled water was used for RI-matching with the quartz window (RI: 1.45). The sample holder was connected to an x-y motorized translation stage (XY MS-2000, Applied Scientific Instrumentation) for sample translation during imaging. To remove air

326 gaps between the quartz window of the sample holder and irregular-shaped tissue specimen,
327 the specimen was partially immersed in the RI-matching solution and light pressure was
328 applied on the top of the specimen. In the imaging arm, emission light was collected by the
329 imaging objective lens (MY20X-804, Mitutoyo) through the liquid prism, spectrally
330 separated into two channels by a dichroic mirror (T425lpxr, Chroma), and collected at two
331 sCMOS cameras (pco-edge 4.2, PCO) after passing through a tube lens (AC254-200-A,
332 Thorlabs), respectively. SHG light was collected in the short pass channel with an emission
333 filter (ET376/30x, Chroma), and fluorescence was collected in the long pass channel with an
334 emission filter (ET680SP, Chroma). Both fluorescence and SHG images were simultaneously
335 acquired with individual gain control.

336 **Human skin cancer specimen collection and imaging protocol**

337 Fresh skin cancer specimens were collected under the Institutional Review Board (IRB) of
338 Yonsei University, Severance Hospital, approved protocol (approval # 4-2021-0128). The
339 study was conducted according to the Declaration of Helsinki Principles. OT-TP-LSM
340 imaging was conducted within 12 h post-excision. Patient information was deidentified.
341 Before imaging, fresh skin specimens were cut cross-sectionally to approximately 4 mm
342 thickness and topically instilled with 400 μg/mL proflavine solution (Sigma) for 5 min, and
343 then rinsed in phosphate-buffered saline. OT-TP-LSM imaging was conducted in 3D on the
344 sectioned surface. After imaging, the skin specimens were fixed and processed for
345 histopathological evaluation with H&E stained slides. Microscopic images were obtained by
346 using a wide-field microscope (Leica Z16 APO, Leica Microsystems).

347 **Human pancreatic and prostate cancer specimen collection and imaging protocol**

348 Formalin-fixed, paraffin-embedded (FFPE) tissue blocks of pancreatic and prostate cancers
349 were collected under approval (approval #, 2021-0393) from the IRB of Asan Medical Center,
350 University of Ulsan College of Medicine. 4 μm thickness sections were made for H&E

351 stained slides, and the remaining blocks were used for OT-TP-LSM imaging. The FFPE
352 tissue blocks were deparaffinized with xylene (99%, Daejung) solution overnight, 1:1 xylene-
353 100% methanol (Optima grade, Fisher scientific) mixture solution for 1 h with shaking,
354 followed by sequentially decreasing the methanol concentration in the xylene and methanol
355 mixture to 90%, 80%, and 50% for 1 h each. After deparaffinization, specimens were stained
356 with 80 μg/mL PI solution (Sigma) for 5 min, and then OT-TP-LSM imaging was conducted
357 on the sectioned surface.

358 **Virtual H&E staining of OT-TP-LSM via deep learning network**

359 CycleGAN is an unsupervised deep learning network without the need for well-aligned image
360 pairs [38] and was used for style transfer of OT-TP-LSM images to virtual H&E images [44-
361 46]. CycleGAN model consisted of two generators (G: real OT-TP-LSM → fake H&E and
362 F: real H&E → fake OT-TP-LSM), and two corresponding discriminators ($D_{OT\text{-}TP\text{-}LSM}$ and
363 $D_{H\&E}$) to identify each fake image (Figure 6 - figure supplement 1). Cycle-consistent loss was
364 combined with adversarial loss to prevent the well-known problem of mode collapse, where
365 all input images mapped to the same output images [38]. For CycleGAN training, PI-labeled
366 OT-TP-LSM and real H&E images were collected from pancreas specimens, including each
367 of normal, premalignant lesions, and cancer. Collected images were cropped into 512 × 512
368 pixels patch images, and augmented by applying rotation (90°, 180°, 270°) and flip (vertical,
369 horizontal). The total training dataset was 14,322 and 22,644 patches for OT-TP-LSM and
370 H&E, respectively. Adam solver was used as an optimizer [47]. Hyper-parameters were set
371 with a batch size of 1 and an initial learning rate of 0.0002 and 100 epochs. Once the training
372 was completed, generator G was used to transform OT-TP-LSM patches into virtual H&E
373 ones.

374

Acknowledgments

This work was supported in part by the National Research Foundation (NRF) grant funded by the Korea government (NRF-2020R1A2C3009309); and the Korea Medical Device Development Fund (KMDF) grant funded by the Korean government (Project Number: 9991006749, KMDF_PR_20200901_0076).

Conflict of interest statements

No conflicts of interest were declared.

References

1. Liu JTC, Glaser AK, Bera K, *et al*. Harnessing non-destructive 3D pathology. *Nat Biomed Eng* 2021; **5:** 203-218.
2. Almagro J, Messal HA, Thin MZ, *et al*. Tissue clearing to examine tumour complexity in three dimensions. *Nat Rev Cancer* 2021; **21:** 718-730.
3. Bishop KW, Maitland KC, Rajadhyaksha M, *et al*. In vivo microscopy as an adjunctive tool to guide detection, diagnosis, and treatment. *J Biomed Opt* 2022; **27:** 040601.
4. Serafin R, Koyuncu C, Xie W, *et al*. Nondestructive 3D pathology with analysis of nuclear features for prostate cancer risk assessment. *J Pathol* 2023; **260:** 390-401.
5. Filler TJ, Peuker ET. Reflection contrast microscopy (RCM): a forgotten technique? *J Pathol* 2000; **190:** 635-638.
6. van Royen ME, Verhoef EI, Kweldam CF, *et al*. Three-dimensional microscopic analysis of clinical prostate specimens. *Histopathology* 2016; **69:** 985-992.

7. Verhoef EI, van Cappellen WA, Slotman JA, *et al*. Three-dimensional analysis reveals two major architectural subgroups of prostate cancer growth patterns. *Modern Pathol* 2019; **32:** 1032-1041.

8. Yoshitake T, Giacomelli MG, Cahill LC, *et al*. Direct comparison between confocal and multiphoton microscopy for rapid histopathological evaluation of unfixed human breast tissue. *J Biomed Opt* 2016; **21:** 126021.

9. Tao YK, Shen DJ, Sheikine Y, *et al*. Assessment of breast pathologies using nonlinear microscopy. *P Natl Acad Sci USA* 2014; **111:** 15304-15309.

10. Baugh LM, Liu ZY, Quinn KP, *et al*. Non-destructive two-photon excited fluorescence imaging identifies early nodules in calcific aortic-valve disease. *Nature Biomedical Engineering* 2017; **1:** 914-924.

11. Patel KB, Liang WX, Casper MJ, *et al*. High-speed light-sheet microscopy for the in-situ acquisition of volumetric histological images of living tissue. *Nature Biomedical Engineering* 2022; **6:** 569-583.

12. Voleti V, Patel KB, Li WZ, *et al*. Real-time volumetric microscopy of in vivo dynamics and large-scale samples with SCAPE 2.0. *Nat Methods* 2019; **16:** 1054-1062.

13. McGorty R, Liu H, Kamiyama D, *et al*. Open-top selective plane illumination microscope for conventionally mounted specimens. *Opt Express* 2015; **23:** 16142-16153.

14. Glaser AK, Reder NP, Chen Y, *et al*. Light-sheet microscopy for slide-free non-destructive pathology of large clinical specimens. *Nature Biomedical Engineering* 2017; **1:** 0084.

15. Glaser AK, Bishop KW, Barner LA, *et al*. A hybrid open-top light-sheet microscope for versatile multi-scale imaging of cleared tissues. *Nat Methods* 2022; **19:** 613-619.

16. Gao G, Miyasato D, Barner LA, *et al*. Comprehensive Surface Histology of Fresh Resection Margins With Rapid Open-Top Light-Sheet (OTLS) Microscopy. *Ieee T Bio-Med Eng* 2023; **70:** 2160-2171.

17. Denk W, Strickler JH, Webb WW. Two-photon laser scanning fluorescence microscopy. *Science* 1990; **248:** 73-76.

18. So PTC, Dong CY, Masters BR, *et al*. Two-photon excitation fluorescence microscopy. *Annu Rev Biomed Eng* 2000; **2:** 399-429.

19. Helmchen F, Denk W. Deep tissue two-photon microscopy. *Nat Methods* 2005; **2:** 932-940.

20. Zipfel WR, Williams RM, Christie R, *et al*. Live tissue intrinsic emission microscopy using multiphoton-excited native fluorescence and second harmonic generation. *Proc Natl Acad Sci U S A* 2003; **100:** 7075-7080.

21. Fast A, Lal A, Durkin AF, *et al*. Fast, large area multiphoton exoscope (FLAME) for macroscopic imaging with microscopic resolution of human skin. *Sci Rep* 2020; **10:** 18093.

22. Park WY, Kim B, Chun JH, *et al*. High-contrast visualization of human skin cancers with combined reflectance confocal and moxifloxacin-based two-photon microscopy: An ex vivo study. *Lasers Surg Med* 2022; **54:** 1226-1237.

23. Fahrbach FO, Gurchenkov V, Alessandri K, *et al*. Light-sheet microscopy in thick media using scanned Bessel beams and two-photon fluorescence excitation. *Opt Express* 2013; **21:** 13824-13839.

24. Mahou P, Vermot J, Beaurepaire E, *et al*. Multicolor two-photon light-sheet microscopy. *Nat Methods* 2014; **11:** 600-601.

25. Wolf S, Supatto W, Debregeas G, *et al*. Whole-brain functional imaging with two-photon light-sheet microscopy. *Nat Methods* 2015; **12:** 379-380.

26. Maioli V, Boniface A, Mahou P, *et al*. Fast in vivo multiphoton light-sheet microscopy with optimal pulse frequency. *Biomed Opt Express* 2020; **11:** 6012-6026.

27. de Vito G, Turrini L, Mullenbroich C, *et al*. Fast whole-brain imaging of seizures in zebrafish larvae by two-photon light-sheet microscopy. *Biomed Opt Express* 2022; **13:** 1516-1536.

28. Planchon TA, Gao L, Milkie DE, *et al*. Rapid three-dimensional isotropic imaging of living cells using Bessel beam plane illumination. *Nat Methods* 2011; **8:** 417-423.

29. Fan JL, Rivera JA, Sun W, *et al*. High-speed volumetric two-photon fluorescence imaging of neurovascular dynamics. *Nat Commun* 2020; **11:** 6020.

30. Rieger AM, Hall BE, Le TL, *et al*. Conventional apoptosis assays using propidium iodide generate a significant number of false positives that prevent accurate assessment of cell death. *J Immunol Methods* 2010; **358:** 81-92.

31. Niu JF, Li CM, Wu HH, *et al*. Propidium iodide (PI) stains Nissl bodies and may serve as a quick marker for total neuronal cell count. *Acta Histochem* 2015; **117:** 182-187.

32. Lemaire K, Chimienti F, Schuit F. Zinc transporters and their role in the pancreatic β - cell. *Journal of Diabetes Investigation* 2012; **3:** 202-211.

33. Hruban RH, Adsay NV, Albores-Saavedra J, *et al*. Pancreatic intraepithelial neoplasia: a new nomenclature and classification system for pancreatic duct lesions. *Am J Surg Pathol* 2001; **25:** 579-586.

34. McGinnis T, Bantis LE, Madan R, *et al*. Survival Outcomes of Pancreatic Intraepithelial Neoplasm (PanIN) versus Intraductal Papillary Mucinous Neoplasm (IPMN) Associated Pancreatic Adenocarcinoma. *J Clin Med* 2020; **9:** 3102.

35. Adsay NV, Bandyopadhyay S, Basturk O, *et al*. Chronic pancreatitis or pancreatic ductal adenocarcinoma? *Semin Diagn Pathol* 2004; **21:** 268-276.

36. Drifka CR, Tod J, Loeffler AG, *et al*. Periductal stromal collagen topology of pancreatic ductal adenocarcinoma differs from that of normal and chronic pancreatitis. *Modern Pathol* 2015; **28:** 1470-1480.

37. Ray A, Callaway MK, Rodriguez-Merced NJ, *et al*. Stromal architecture directs early dissemination in pancreatic ductal adenocarcinoma. *JCI Insight* 2022; **7:** e150330.

38. Zhu JY, Park T, Isola P, *et al*. Unpaired Image-to-Image Translation using Cycle-Consistent Adversarial Networks. *Ieee I Conf Comp Vis* 2017; 2242-2251.

39. Olarte OE, Licea-Rodriguez J, Palero JA, *et al*. Image formation by linear and nonlinear digital scanned light-sheet fluorescence microscopy with Gaussian and Bessel beam profiles. *Biomed Opt Express* 2012; **3:** 1492-1505.

40. Young PA, Clendenon SG, Byars JM, *et al*. The effects of refractive index heterogeneity within kidney tissue on multiphoton fluorescence excitation microscopy. *J Microsc-Oxford* 2011; **242:** 148-156.

41. Aoyagi Y, Kawakami R, Osanai H, *et al*. A Rapid Optical Clearing Protocol Using 2,2'-Thiodiethanol for Microscopic Observation of Fixed Mouse Brain. *Plos One* 2015; **10:** e0116280.

42. Minamikawa T, Hashimoto M, Fujita K, *et al*. Multi-focus excitation coherent anti-Stokes Raman scattering (CARS) microscopy and its applications for real-time imaging. *Opt Express* 2009; **17:** 9526-9536.

43. Chen X, Zong W, Li R, *et al*. Two-photon light-sheet nanoscopy by fluorescence fluctuation correlation analysis. *Nanoscale* 2016; **8:** 9982-9987.

44. Chen Z, Yu W, Wong IHM, *et al*. Deep-learning-assisted microscopy with ultraviolet surface excitation for rapid slide-free histological imaging. *Biomed Opt Express* 2021; **12:** 5920-5938.

45. Cao R, Nelson SD, Davis S, *et al*. Label-free intraoperative histology of bone tissue via deep-learning-assisted ultraviolet photoacoustic microscopy. *Nat Biomed Eng* 2023; **7:** 124-134.

46. Abraham T, Shaw A, O'Connor D, *et al*. Slide-free MUSE microscopy to H&E histology modality conversion via unpaired image-to-image translation GAN Models. v1. arXiv.org 2020. Available from: https://arxiv.org/abs/2008.08579. Accessed: [14 August 2023]. Not peer-reviewed.

47. Kingma DP, Ba J. Adam: A method for stochastic optimization. v9. arXiv.org 2014. Available from: https://arxiv.org/abs/1412.6980. Accessed: [14 August 2023]. Not peer-reviewed.

504 **Figure legends**

505 **Figure 1. Schematics and characteristics of open-top two-photon light sheet microscopy**
506 **(OT-TP-LSM).** (A) Overall design of OP-TP-LSM. L: lens; M: mirror; DM: dichroic mirror;
507 SPF: short pass filter; BPF: band pass filter; OBJ: objective lens. (B) Detailed schematic of
508 the sample interface, including the liquid prism filled with refractive index (RI)-matching
509 solution. (C) Illustration of sequential light sheet imaging with stepwise lateral translation.
510 (D) Image resolution characterized by three-dimensional (3D) imaging of 0.5 μm fluorescent
511 microspheres. (E) Imaging depth characterized by imaging a proflavine-labeled fresh human
512 skin specimen in comparison with that of one-photon light sheet microscopy (1PLSM) using
513 Gaussian excitation sheet.

514 **Figure 2. 3D OT-TP-LSM images of fresh human skin cancer (basal cell carcinoma,**
515 **BCC) specimens.** (A) Large-sectional OT-TP-LSM and hematoxylin and eosin (H&E)
516 stained slide images of a BCC case 1. (B and C) Two magnified images of regions of interest
517 (ROIs) with corresponding H&E images. ROI 1 and 2 were in the epidermis and superficial
518 dermis and the BCC region below, respectively. (D) Large-sectional OT-TP-LSM and H&E
519 images of a BCC case 2. (E and F) Two magnified images of ROIs with corresponding H&E
520 images. ROI 3 and 4 were in eccrine and sebaceous glands, respectively. Superficial cell
521 layers of both glands are marked with a white arrow. In the OT-TP-LSM images, proflavine
522 fluorescence and second harmonic generation (SHG) are displayed in green and blue,
523 respectively.

524 **Figure 3. 3D OT-TP-LSM images of two human pancreas specimens: normal and**
525 **premalignant lesion.** (A) Large-area OT-TP-LSM and H&E stained images of normal
526 human pancreas. (B and C) Magnified two-depth OT-TP-LSM images of ROI 1 and 2 in the
527 normal pancreas and the corresponding H&E stained slide images. ROI 1 and 2 were on the
528 acini and islets of Langerhans and the pancreatic duct, respectively. 3D morphological

529 change of the duct was marked with a white arrow. (D) Large-area OT-TP-LSM and H&E
530 stained images of a pancreatic premalignant lesion. Red box indicates the intraductal
531 papillary mucinous neoplasm (IPMN). (E) Magnified two-depth OT-TP-LSM images of ROI
532 3 and corresponding H&E image of pancreatic intraepithelial neoplasia (PanIN). 3D
533 morphological change of papillary in the PanIN was marked with a cyan arrow. In OT-TP-
534 LSM images, propidium iodide (PI)-labeled cells and SHG-emitting collagen are displayed in
535 green and blue, respectively.

536 **Figure 4. 3D OT-TP-LSM images of human pancreatic ductal adenocarcinoma (PDAC).**
537 (A) Large-area OT-TP-LSM and H&E stained slide images of PDAC arising from IPMN
538 specimen. Pink solid line indicates the IPMN area. (B and C) Magnified two-depth OT-TP-
539 LSM images of ROI 1 and 2 in the PDAC region and the corresponding H&E stained images.
540 ROI 1 was on the PDAC, and ROI 2 was on the boundary region between nonneoplastic
541 pancreatitis and PDAC, respectively. A nonneoplastic duct and a PDAC were marked with
542 green and red arrows, respectively. A white dashed line indicated the boundary between
543 nonneoplastic pancreatitis and PDAC. In the OT-TP-LSM images, PI-labeled cells and SHG-
544 emitting collagen are displayed in green and blue, respectively.

545 **Figure 5. 3D OT-TP-LSM images of human prostate specimens: benign and**
546 **adenocarcinoma.** (A) Large-area OT-TP-LSM and H&E stained slide images of a benign
547 prostate specimen. (B) Magnified two-depth OT-TP-LSM images of ROI 1 in the benign
548 gland and a corresponding H&E image. (C) Large-area OT-TP-LSM and H&E images of a
549 prostatic cancer specimen. A white solid line indicated the boundary between
550 adenocarcinoma and benign regions. (D) Magnified two-depth OT-TP-LSM images of ROI 2
551 in adenocarcinoma glands and a corresponding H&E image. In OT-TP-LSM images, PI-
552 labeled cells and SHG-emitting collagen were visualized in green and blue, respectively.

553 **Figure 6. Style transfer of OT-TP-LSM images for virtual H&E by cycle-consistent**
554 **generational adversarial networks (CycleGAN).** (A and C) Large-area virtual H&E images
555 and corresponding H&E stained slide images of PanIN and PDAC specimens, respectively.
556 (B and D) Magnified virtual H&E images and corresponding H&E stained images of PanIN
557 and PDAC, respectively.
558
559 **Supplementary figure legends**
560 **Figure 1 - figure supplement 1. Detail optical configuration of illumination arm in open-**
561 **top two-photon light sheet microscopy (OT-TP-LSM).** (A) Illustration of beam path at Y-
562 Z' plan. L: lens, BF: barrier filter, AL: axicon lens, SM: scanning mirror, OBJ: objective lens.
563 Two-photon light sheet with extended depth of field (DOF) was generated by scanning a
564 Bessel beam in the Y-axis direction rapidly. (B) Illustration of beam path at Z-X plan. (C)
565 Magnified image and designed dimension of the Bessel beam based light sheet. The
566 excitation light sheet was designed to have a DOF of 180 μm with a thickness of 0.9 μm.
567 **Figure 3 - figure supplement 1. Comparison of imaging depth between propidium iodide**
568 **(PI) and proflavine in human pancreas.** (A) 45° oblique OT-TP-LSM image of pancreas
569 specimens after PI cell labeling. (B) 45° oblique OT-TP-LSM image of pancreas specimens
570 after proflavine cell labeling. PI labeling enabled the deeper imaging up to approximately 55
571 μm from the surface owing to its relatively long peak emission wavelength compared to
572 proflavine. Both pancreas specimens were incubated with PI and proflavine for 5 mins,
573 respectively.
574 **Figure 3 - figure supplement 2. PI cell staining characteristics in human pancreas.** (A)
575 OT-TP-LSM image of acinar cell structures in normal pancreas specimens after PI cell
576 labeling and corresponding H&E image. (B) OT-TP-LSM image of pancreatic intraepithelial
577 neoplasia (PanIN) structures in premalignant pancreas after PI cell labeling and

578 corresponding H&E image. In OT-TP-LSM images, PI fluorescence was displayed in green
579 color. PI showed nuclear and cytoplasmic labeling properties of cells in both acini and
580 neoplastic structures. Cell nuclei were identified with relatively strong and weak fluorescence
581 in the membrane and core, respectively.

582 **Figure 6 - figure supplement 1. Cycle-consistent generational adversarial networks**
583 **(CycleGAN) workflow for style transfer of OT-TP-LSM image to virtual hematoxylin**
584 **and eosin (H&E) image.** Real OT-TP-LSM image and real H&E image were assigned as $\boldsymbol{x}$
585 and $\boldsymbol{y}$, and the corresponding fake image is additionally marked with a prime. The generator
586 G transformed the real OT-TP-LSM image into a fake virtual H&E-stained image. Generator
587 F transformed the real H&E image into a fake OT-TP-LSM image. The discriminator $D\boldsymbol{x}$
588 classifies real OT-TP-LSM image $\boldsymbol{x}$ and fake OT-TP-LSM image $\boldsymbol{x}'$. The discriminator $D\boldsymbol{y}$
589 classifies real H&E image $\boldsymbol{y}$ and fake virtual H&E image $\boldsymbol{y}'$. Both Cycle-consistent loss and
590 adversarial loss were used as the loss function, which was to guarantee the performance of
591 inverse transform from G and F by preserving the morphological features of real images.

592

593 **Video legend**

594 **Video 1.** Three-dimensional (3D) visualization of basal cell carcinoma (BCC) structures and
595 normal cell structures.

Figure 1

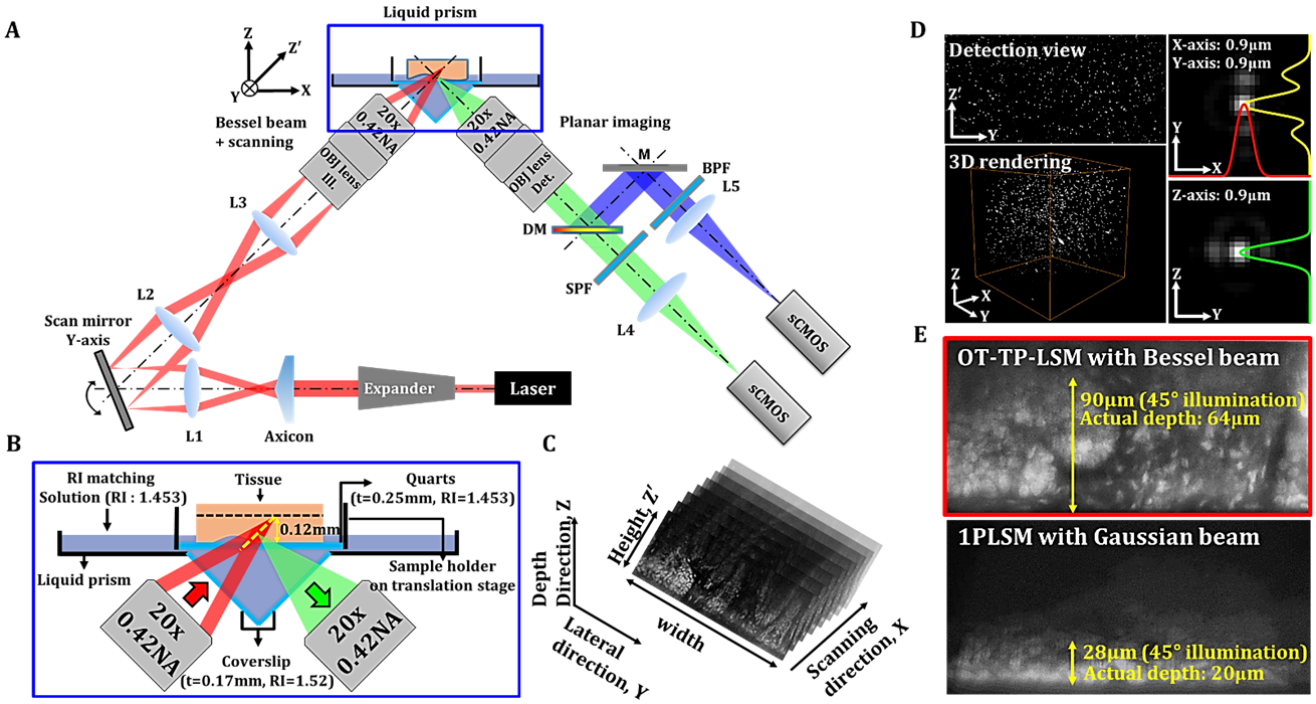
A
Liquid prism
Z
Z'
Y
X
Bessel beam
+ scanning
20x
0.42NA
OBJ lens
Ill.
20x
0.42NA
OBJ lens
Det.
Planar imaging
M
BPF
L5
L3
DM
SPF
L2
L4
Scan mirror
Y-axis
sCMOS
sCMOS
Expander
Laser
L1
Axicon
B
RI matching
Solution (RI : 1.453)
Tissue
Quarts
(t=0.25mm, RI=1.453)
0.12mm
Liquid prism
Sample holder
on translation stage
20x
0.42NA
20x
0.42NA
Coverslip
(t=0.17mm, RI=1.52)
C
Depth
Direction, Z
Height, Z'
Lateral
direction, Y
width
Scanning
direction, X
D
Detection view
X-axis: 0.9μm
Y-axis: 0.9μm
3D rendering
Z-axis: 0.9μm
E
OT-TP-LSM with Bessel beam
90μm (45° illumination)
Actual depth: 64μm
1PLSM with Gaussian beam
28μm (45° illumination)
Actual depth: 20μm

Figure 1 - figure supplement 1

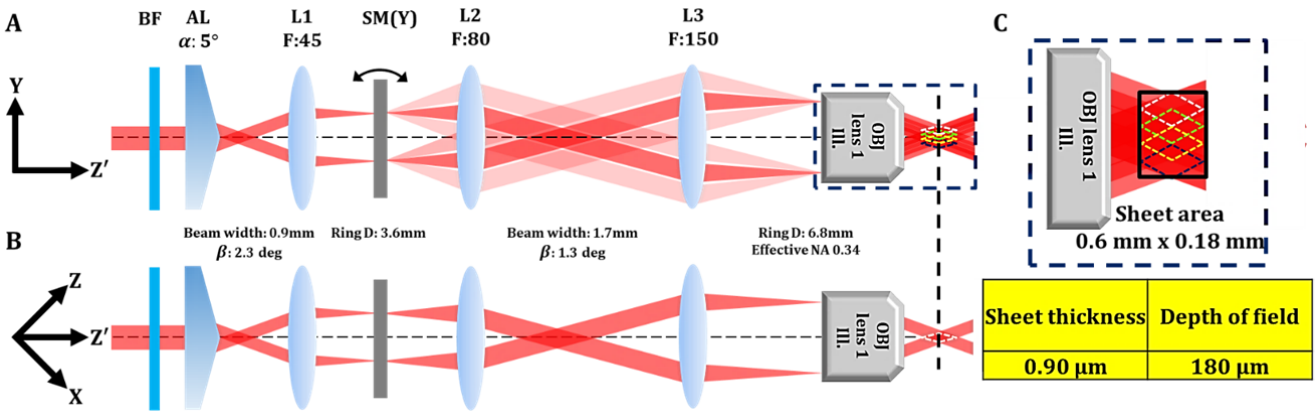

Figure 2

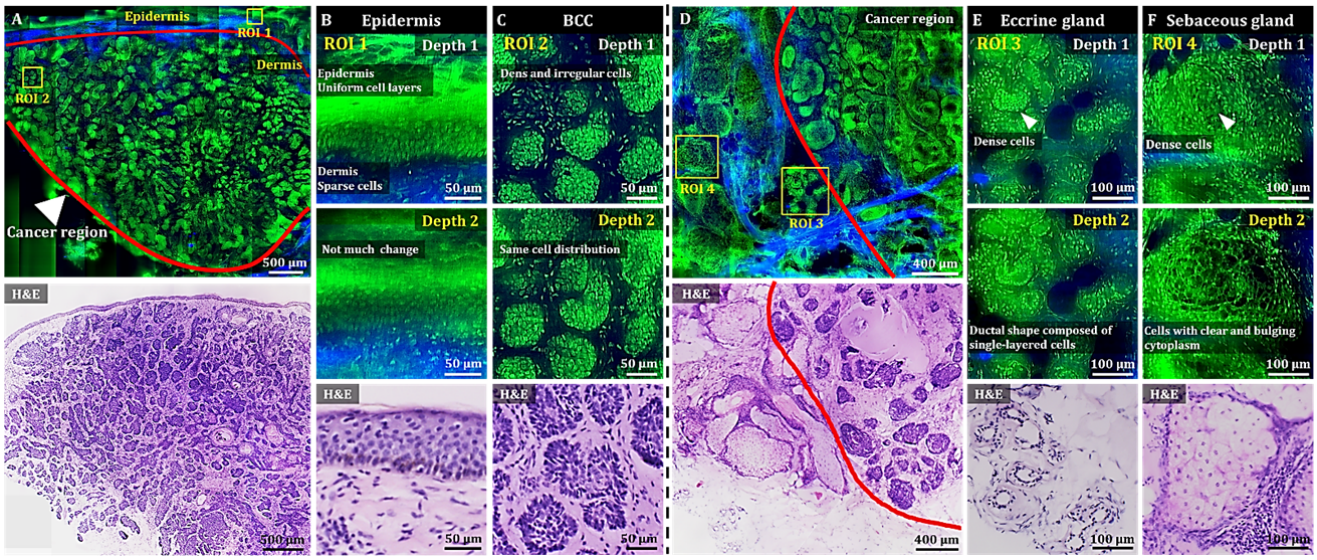
A
Epidermis
ROI 1
Dermis
ROI 2
Cancer region
500 µm
H&E
500 µm
B Epidermis
ROI 1
Depth 1
Epidermis
Uniform cell layers
Dermis
Sparse cells
50 µm
Depth 2
Not much change
50 µm
H&E
50 µm
C BCC
ROI 2
Depth 1
Dens and irregular cells
50 µm
Depth 2
Same cell distribution
50 µm
H&E
50 µm
D
Cancer region
ROI 4
ROI 3
400 µm
H&E
400 µm
E Eccrine gland
ROI 3
Depth 1
Dense cells
100 µm
Depth 2
Ductal shape composed of single-layered cells
100 µm
H&E
100 µm
F Sebaceous gland
ROI 4
Depth 1
Dense cells
100 µm
Depth 2
Cells with clear and bulging cytoplasm
100 µm
H&E
100 µm

Figure 3

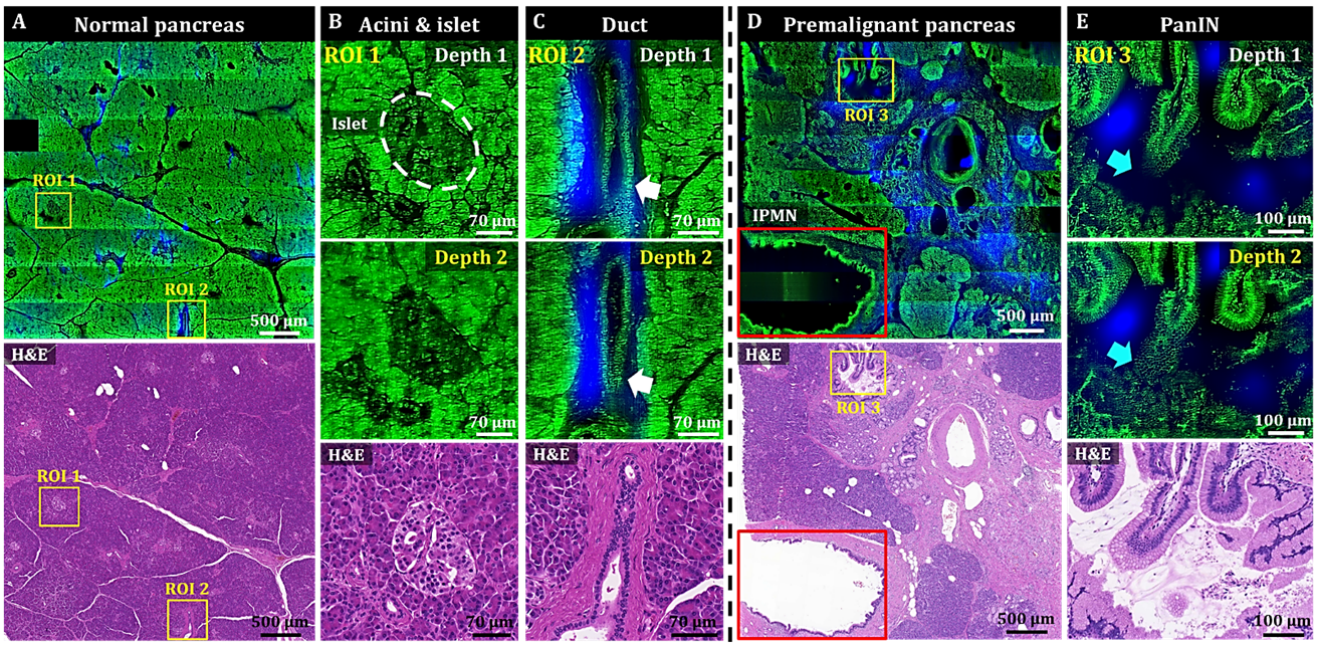
A
Normal pancreas
ROI 1
ROI 2
500 µm
H&E
ROI 1
ROI 2
500 µm
B
Acini & islet
ROI 1
Depth 1
Islet
70 µm
Depth 2
70 µm
H&E
70 µm
C
Duct
ROI 2
Depth 1
70 µm
Depth 2
70 µm
H&E
70 µm
D
Premalignant pancreas
ROI 3
IPMN
500 µm
H&E
ROI 3
500 µm
E
PanIN
ROI 3
Depth 1
100 µm
Depth 2
100 µm
H&E
100 µm

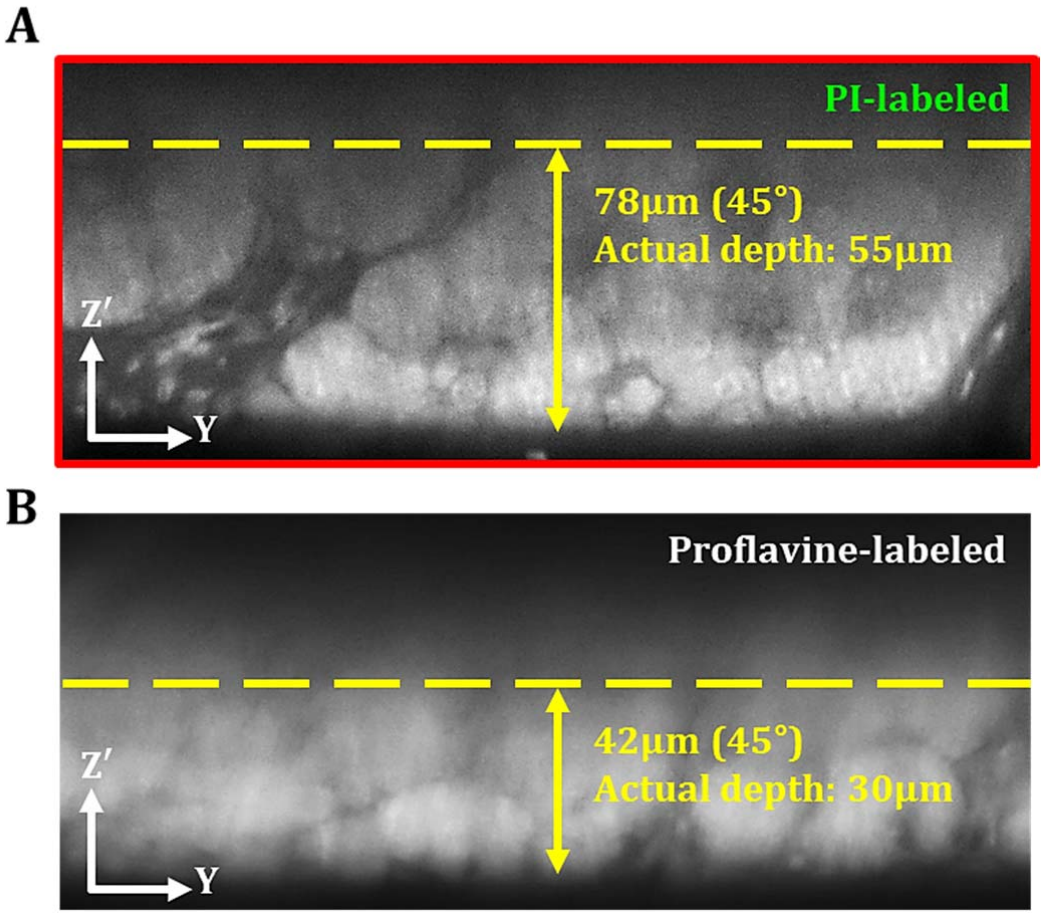
A
PI-labeled
78µm (45°)
Actual depth: 55µm
Z′
Y
B
Proflavine-labeled
42µm (45°)
Actual depth: 30µm
Z′
Y

Figure 3 - figure supplement 2

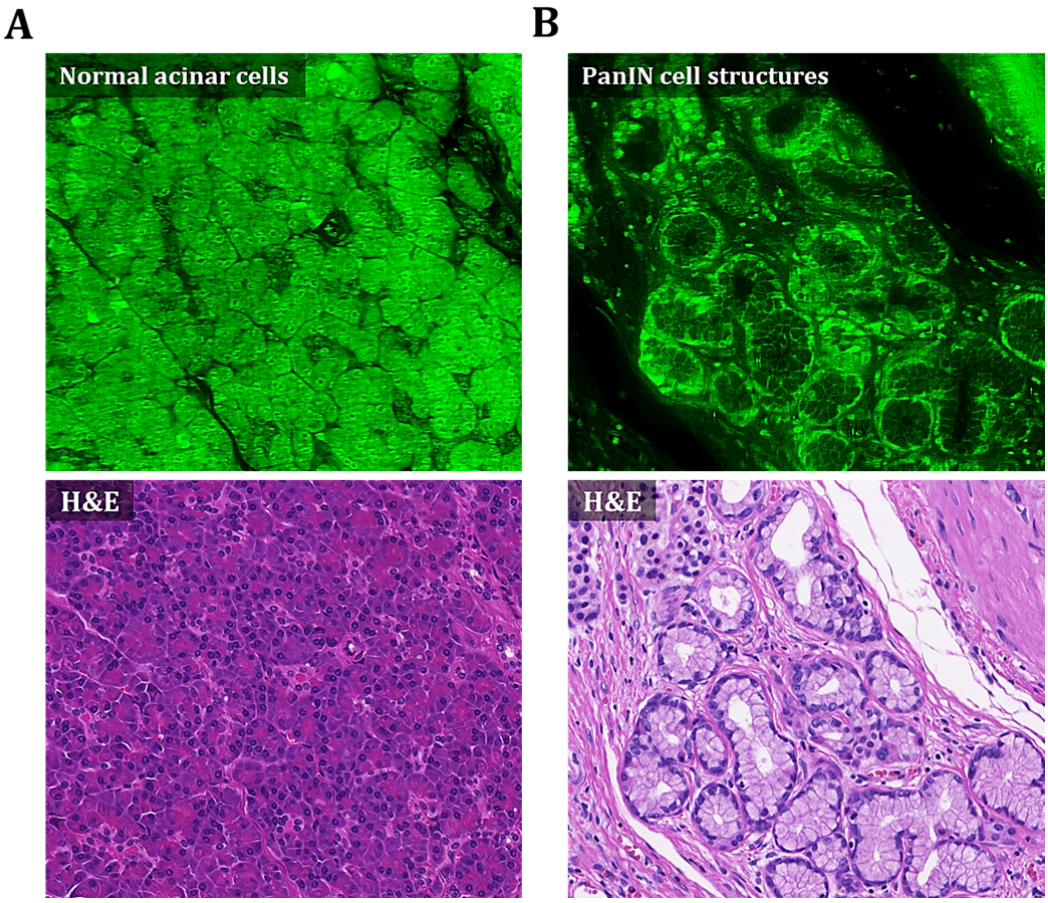

Figure 4

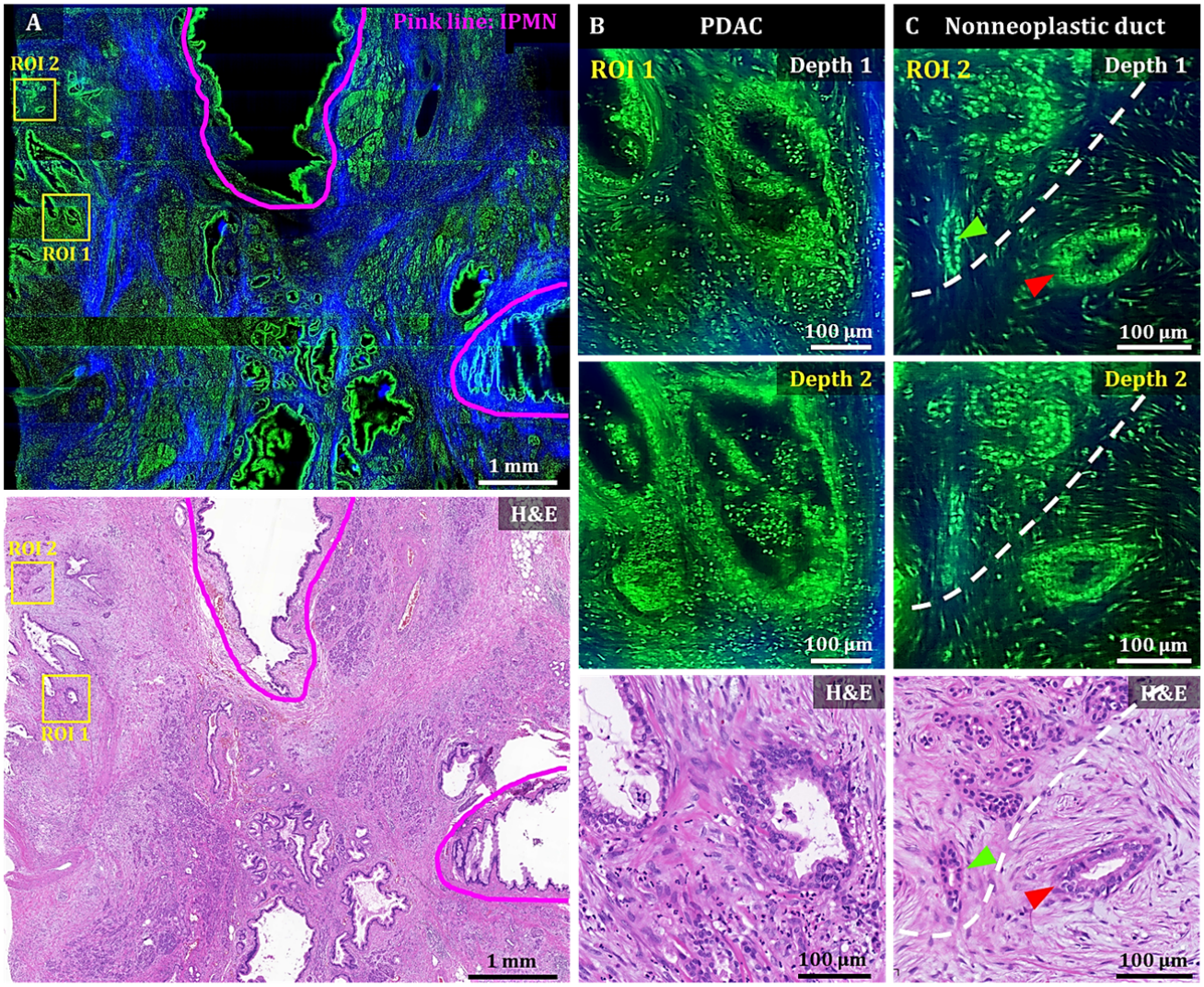
A
Pink line: IPMN
ROI 2
ROI 1
1 mm
H&E
ROI 2
ROI 1
1 mm
B
PDAC
ROI 1
Depth 1
100 µm
Depth 2
100 µm
H&E
100 µm
C
Nonneoplastic duct
ROI 2
Depth 1
100 µm
Depth 2
100 µm
H&E
100 µm

Figure 5

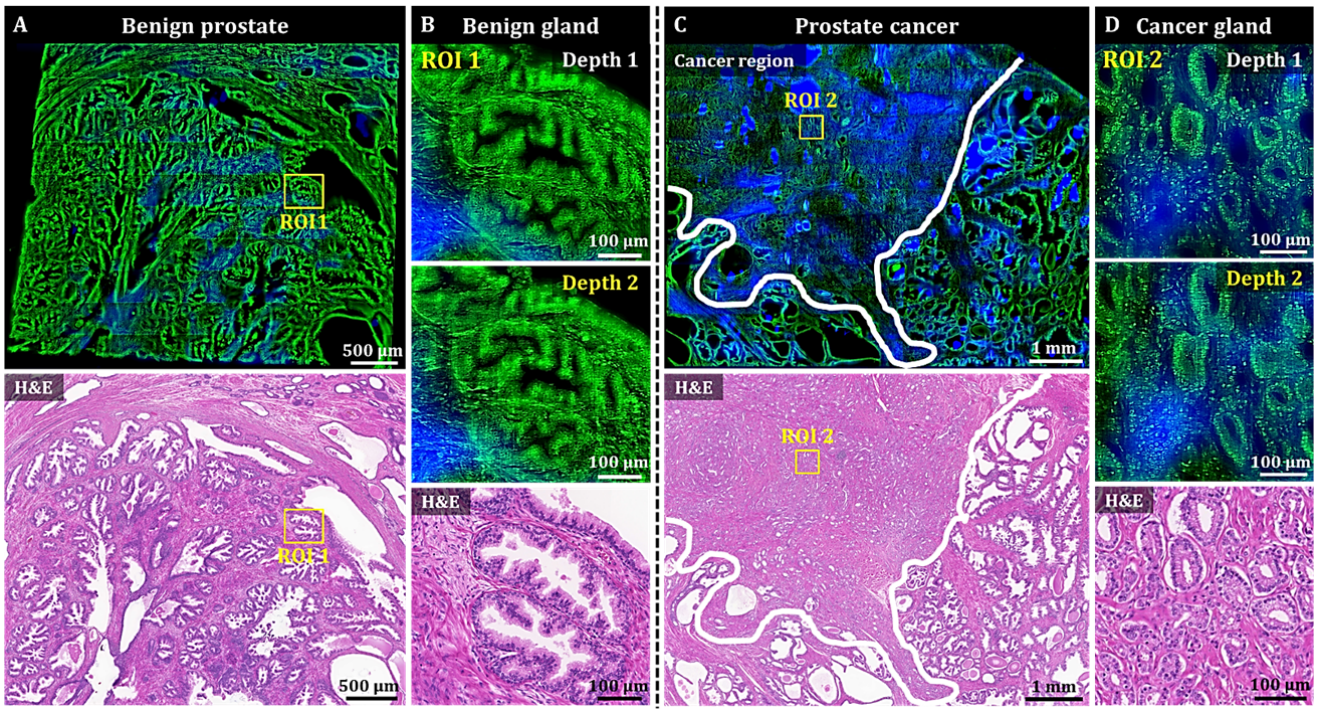
A
Benign prostate
ROI1
500 µm
H&E
ROI 1
500 µm
B
Benign gland
ROI 1
Depth 1
100 µm
Depth 2
100 µm
H&E
100 µm
C
Prostate cancer
Cancer region
ROI 2
1 mm
H&E
ROI 2
1 mm
D
Cancer gland
ROI 2
Depth 1
100 µm
Depth 2
100 µm
H&E
100 µm

Figure 6

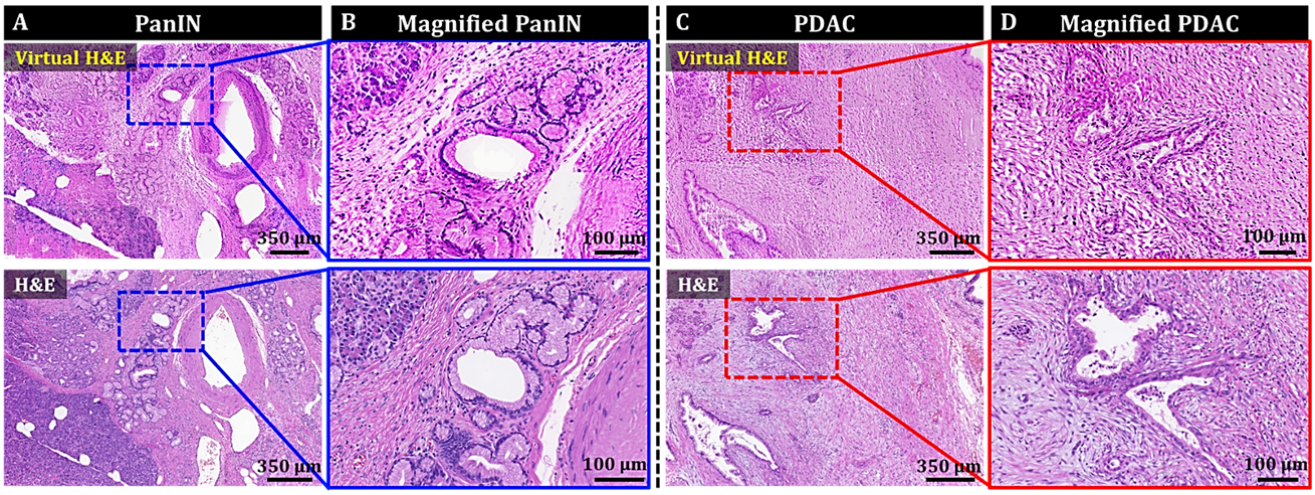
A
PanIN
B
Magnified PanIN
C
PDAC
D
Magnified PDAC
Virtual H&E
H&E
350 µm
100 µm
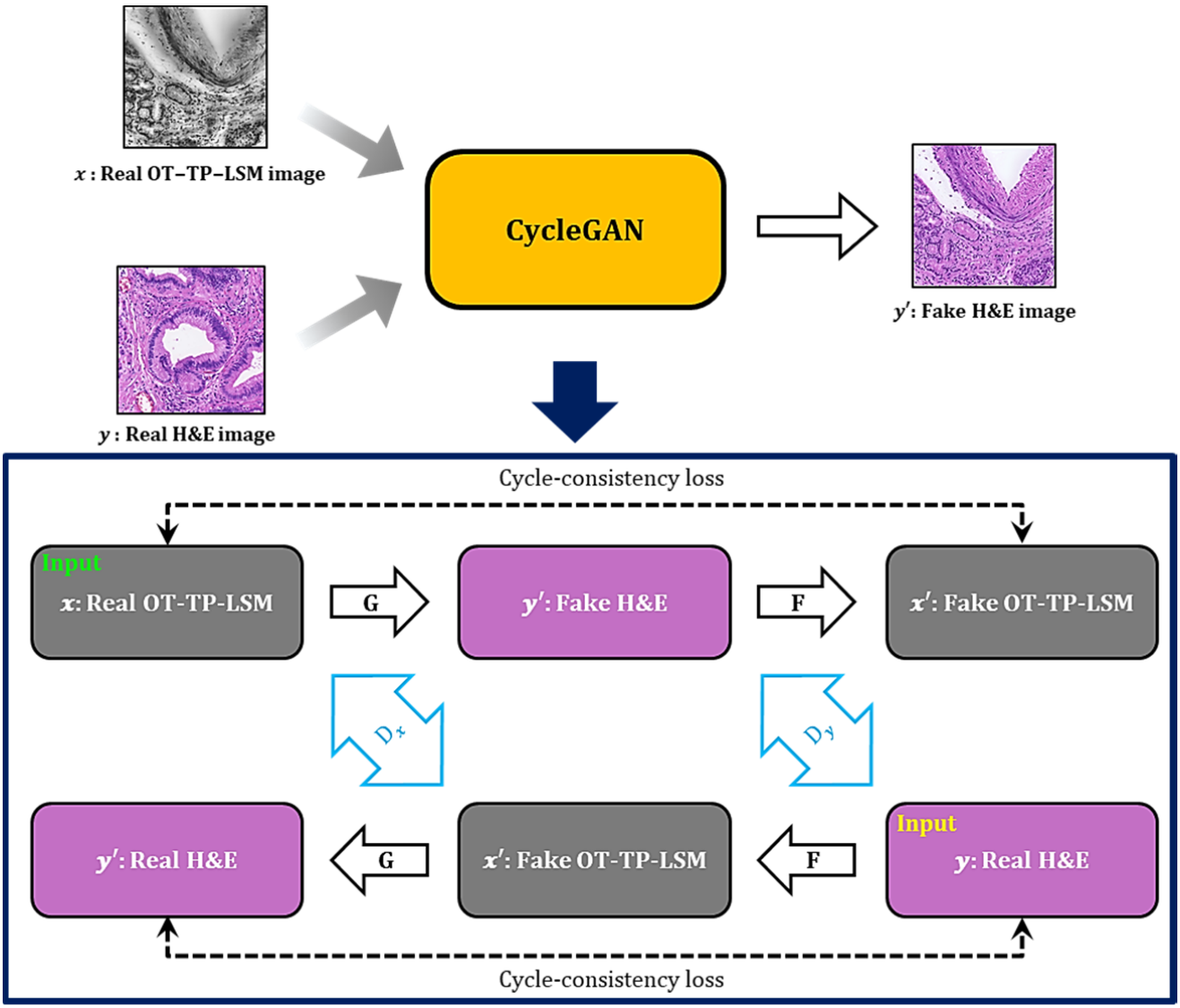
Figure 6 - figure supplement 1